Composite bending-dominated hollow nanolattices: A stiff, cyclable mechanical metamaterial

Biwei Deng [1], Rong Xu [2], Kejie Zhao [2], Yongfeng Lu [3], Sabyasachi Ganguli [4], Gary J. Cheng [1,2,5],*

[1] School of Industrial Engineering, Purdue University, West Lafayette, IN, USA
[2] School of Mechanical Engineering, Purdue University, West Lafayette, IN, USA
[3] Department of Electrical and Computer Engineering, University of Nebraska Lincoln, Lincoln, Nebraska, IN, USA
[4] Advanced Nanoelectronics Branch, Wright-Patterson Air Force Base, Dayton, OH, USA
[5] The Institute of Technological Sciences, Wuhan University, Wuhan, Hubei 430072, China

Manufacturing ultralight and mechanical reliable materials has been a long-time challenge. Ceramic-based mechanical metamaterials provide significant opportunities to reverse their brittle nature and unstable mechanical properties and have great potential as strong, ultralight, and ultrastiff materials. However, the failure of ceramics nanolattice and degradation of strength/modulus with decreasing density are caused by buckling of the struts and failure of the nodes within the nanolattices, especially during cyclic loading. Here, we explore a new class of 3D ceramic-based metamaterials with a high strength–density ratio, stiffness, recoverability, cyclability, and optimal scaling factor. Deformation mode of the fabricated nanolattices has been engineered through the unique material design and architecture tailoring. Bending-dominated hollow nanolattice (B-H-Lattice) structure is employed to take advantages of its flexibility, while a few nanometers of carbonized mussel-inspired bio-polymer (C-PDA) is coherently deposited on ceramics' nanolayer to enable non-buckling struts and bendable nodes during deformation, resulting in reliable mechanical properties and outperforming the current bending-dominated lattices (B-Lattices) and carbon-based cellulose materials. Meanwhile, the structure has comparable stiffness to stretching-dominated lattices (S-Lattices) while with better cyclability and reliability. The B-H-Lattices exhibit high specific stiffness ($>10^6$ Pa·kg^{-1}·m^{-3}), low-density ($\sim$30 kg/m^3), buckling-free recovery at 55% strain, and stable cyclic loading behavior under up to 15% strain. As one of the B-Lattices, the modulus scaling factor reaches 1.27, which is lowest among current B-Lattices. This study suggests that non-buckling behavior and reliable nodes are the key factors that contribute to the outstanding mechanical performance of nanolattice materials. A new concept of engineering the internal deformation behavior of mechanical metamaterial is provided to optimize their mechanical properties in real service conditions.

Introduction

Nature has inspired people to incorporate multiple materials with distinct mechanical properties into a new category of materials: composite. It has affected human's life in numerous applications, such as structural materials [1], heat dissipation [2], medical tools [3], energy storage [4], electronic devices [5], smart robotics [6], etc. Specifically, from a mechanical perspective, when two different materials are organized in a periodic manner, such as lamellar or brick/mortar, their mechanical properties, such as strength, stiffness, and toughness, can be significantly

* Corresponding author at: School of Industrial Engineering, Purdue University, West Lafayette, IN, USA.

E-mail address: Cheng, G.J. (gjcheng@purdue.edu).

boosted [2], overcoming the 'rule of mixtures' [7–9]. Yet, nature materials are internally dense as a bulk. For example, trabecular bone and wood have their unique micro- or nano-scale architectures, which improve their property/mass efficiency, i.e., specific mechanical performance, by reducing their weight [10–13]. Manufacturing of complex micro/nano architectures with composite materials with the least possible mass has been a challenge toward the best reproduction of nature's materials.

With the advancement of 3D printing in micro/nano scale, it becomes possible to manufacture materials with complex internal structures toward boosted mechanical properties [14]. Many novel micro/nano architectures have been built by both composite materials' design and nanoscale 3D architecture tailoring [15–18]. Metal-based (e.g., Ni, Cu) microstructure via electroless plating [19,20], and ceramics (e.g., TiN and Al_2O_3) nanostructures via atomic layer deposition (ALD), were fabricated on 3D truss structures [16,21]. 3D hollow architectures are featured with properties like ultra-light, ultra-stiff, and recoverable, which opened new horizons for 'mechanical metamaterials' [22,23]. There are two major categories of truss structure designs: stretching-dominated lattices (S-Lattices) and bending-dominated lattices (B-Lattices) [12,24]. S-Lattices stand out for their high stiffness [25], as the struts in the structure do not have freedom to rotate or bend due to the high nodal connectivity. However, most S-Lattices are faced with inevitable local buckling under large compressive strains [16–21]. Buckling in lattice materials, although plays a role in recovery of lattices, significantly affects the strength and cyclability of the structure. Contrary to S-Lattices, B-Lattices allow their struts to rotate or bend depending on whether the node is pin-joint or welded. Thus, B-Lattices usually feature with compliance and resistance to impact damage under large strains [26,27]. However, compared with S-Lattices, the stiffness and strength of B-Lattices are lacking for critical structural components. Multiscale hierarchical 3D structures have been fabricated combining bending-dominated design with stretching-dominated structured beams in order to achieve both tensile stability and stiffness, however buckling still exists in the system causing unstable local damages [18].

In addition, due to the challenge of printing multiple materials on complex 3D geometries, material choices of aforementioned 3D architectures are limited. In many cases, only a single type of material can be applied when constructing multiscale 3D structures. Recently, composite material designs have been attempted to incorporate nanoscale architectures. Ceramic nanolayer reinforced graphene aerogels have been demonstrated with enhanced stiffness and superelasticity [28]. However, as aerogels are constructed randomly, the potential to design their mechanical property and other functionalities is limited. On the other hand, ordered core–shell composite architectures have been fabricated by depositing ceramic or metal nanolayers on the surface of the 3D-printed resin template [17,29,30]. In these structures, buckling can be greatly inhibited as the core and the shell have different buckling behavior and restrain each other through their interface. As a result, composite core–shell structures are often brittle when buckling is absent [17,29]. Since the core diameter (~200–300 nm) is larger than the shell thickness (~5–20 nm), the size effect of the ultrathin shell layer and the coupling effect between the core and the shell, which could

significantly enhance the strength, haven't been pushed to the optimal.

Herein, we demonstrate a bending-dominated hollow nanolattice material (B-H-Lattice) with nanolayered struts to realize ultra-low density, high strength, and good recoverability and cyclability. The deformation mode of the fabricated nanolattices has been engineered through the unique material design and architecture tailoring. Bending-dominated hollow nanolattice (B-H-lattice) with bendable nodes is employed to take advantages of its flexibility, while a carbonized polymer nanolayer is deposited coherently on a ceramic nanolayer to enable non-buckling struts during deformation, resulting in better scaling factors and strength/density ratio than the current bending-dominated lattices (B-Lattices) and carbon-based cellulose materials. Unlike the current ceramic lattices, this B-H-Lattice exhibits good recoverability without any buckling behavior. Meanwhile, the composite B-H lattices have comparable stiffness and strength to existing stretching-dominated lattices (S-Lattices) with similar mass densities while with better cyclability and reliability. This approach provides a new way to scalable fabrication of advanced ceramic nanocomposites with engineered mechanical property that is comparable to nature-produced materials.

Results and discussion
Hierarchical hollow microlattices with multi-material nanolayers

The fabricated B-H-Lattice consists of 8 stacks of fourfold symmetrical bow-tie units supported and interconnected by vertical struts (See Figure 1a). The lattice templates are fabricated by interference lithography with UV curable resin. An interior nanolayer of ALD alumina is deposited on the 3D templates followed by an exterior nanolayer of carbonized polydopamine (C-PDA). Detailed fabrication methods can be found in the Supplementary Materials. Polydopamine (PDA) is a mussel-inspired bio-polymer, which can be deposited with aqueous chemical reaction [31]. We choose PDA as the precursor of our coating since it forms a nanolayer conformally on arbitrary surface geometries and its thickness is controllable down to sub-10 nm [32]. Also, since PDA was first used for an adhesion layer [33], the interface between PDA and substrate is robustly bonded, which could prevent the composite nano-layers from potential delamination [34,35]. After the deposition, the resin template was removed by thermal decomposition at 500 °C for one hour. A hollow architecture with nanolayered walls then remains on the glass substrate. Successful deposition of the ALD alumina and C-PDA are confirmed by EDS mapping (Figure S2). The C-PDA nanolayer is also characterized by Raman spectroscopy and X-ray photoelectron spectroscopy (XPS). The Raman spectrum of the nanolayered wall before the furnace carbonization (Figure 1e) shows no distinct peaks. As a comparison, D peak (~1300 cm^{-1}) and G peak (~1600 cm^{-1}) are present on the Raman spectrum of the thermal-processed nanolayered wall. Raman signal of the G peak is mapped on the nanolayered lattice (Figure 1c), showing that C-PDA layer is conformally deposited on the 3D geometry. TEM inspection indicates that the nanolayered wall consists of 15 nm of alumina and 8 nm of C-PDA. The TEM image (Figure 1d) also confirms the tight attachment between the C-PDA and
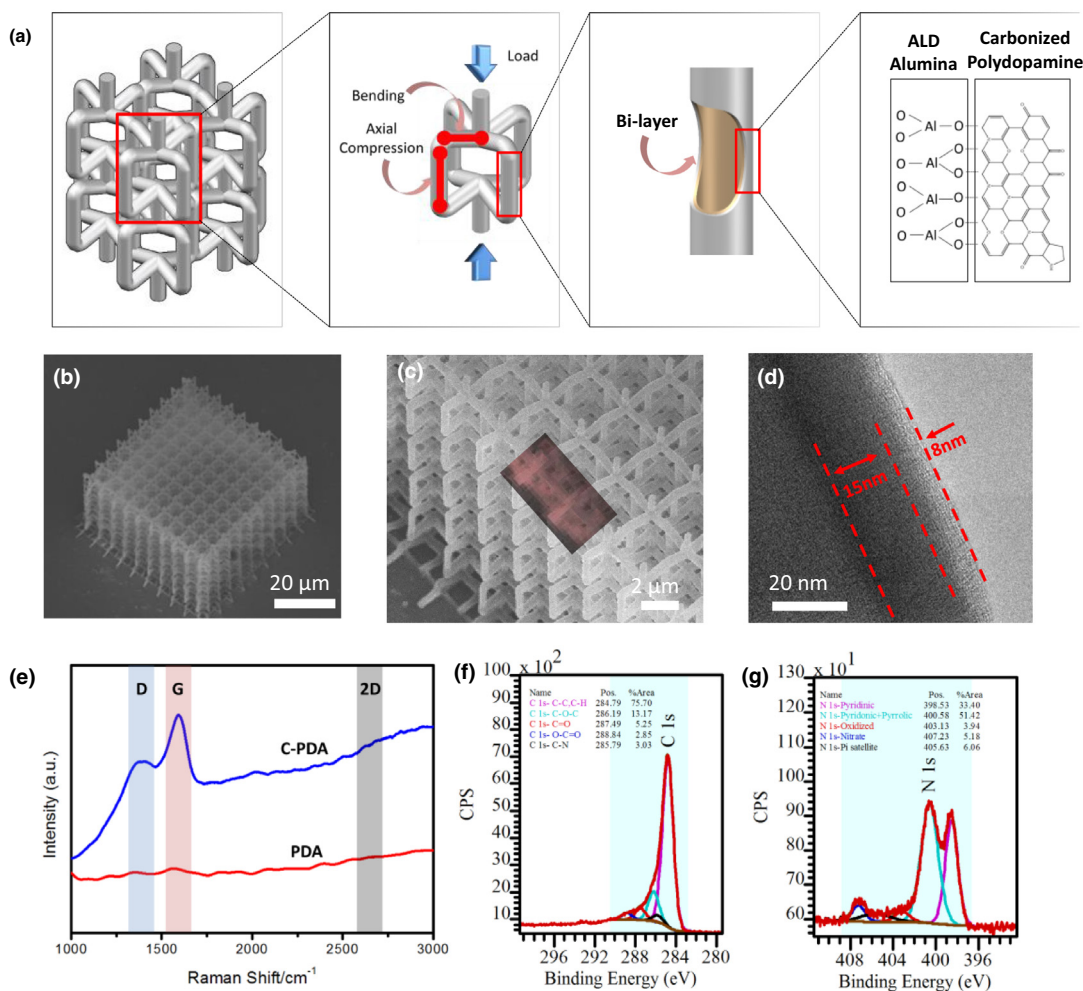
FIGURE 1

Structural design and microstructure of the composite hollow lattice. (a) Illustration of multiscale design of the composite hollow lattice; (b) SEM image from a tilted view of a composite hollow lattice; (c) zoomed SEM image of a composite hollow lattice, with an inserted heatmap of Raman signals from G peak of carbonized polydopamine (C-PDA); (d) TEM image of the tube wall of a hollow strut from the composite hollow lattice, showing that the thickness of alumina nanolayer is 15 nm and that the thickness of C-PDA nanolayer is 8 nm; (e) Raman spectrum of the as-coated polydopamine (PDA) and C-PDA; (f) XPS spectrum of C 1s from C-PDA; (g) XPS spectrum of N 1s from C-PDA.

alumina nanolayers. In Figures 1f & g and S3, the XPS spectra from the nanolayered film further reveals the bonding types in the nanolayers and their interface (See Supplementary Materials for detailed analysis). The functional groups in C-PDA, such as C-O, C-O-C, and C-N, have been reported to enhance the interfacial attachment between the two nanolayers through the formation of hydrogen bonding [36,37]. Even when the nanolayers are bound merely by the Van der Waals force, the friction between the nanolayers can ramp up dramatically if the contact is conformal [38]. As a result, no delamination is observed between alumina and C-PDA during mechanical tests in this study. It is worth noting that the delamination in core–shell components is a problem in several reported 3D composite lattices [29,30].

Recoverability and cyclability of the B-H-Lattice metamaterials
We studied the deformation of the two types of B-H-Lattices, ones with 15-nm alumina nanolayer and ones with 15-nm alumina/8-nm C-PDA nanolayers. The recoverability and cycla-

bility are compared using in-situ SEM compression test (displacement rate: 100 nm/s) and flat punch indentation test (displacement rate: 20 nm/s). In the case of pure alumina B-H-Lattices, as in the SEM images in Figure 2a, when the strain goes beyond elastic range, local "necking" appears near the bottom of the structure. This is caused by the "node bending", which will be discussed in the next section, in bow-tie units, leading to a decrease in horizontal dimensions of the overall lattice. The effective strain of the lattice is concentrated at the bottom right of the lattice where the necking started to develop, as shown in the strain map in Figure 2a. From the displacement vectors in the strain map, the upper part of the lattice, where the effective strain is close to 0, is moving down along Z direction. Notably, the buckling of individual hollow struts is predominant in the necking part of the lattice. Because of the severe local buckling, the ceramic structure cannot fully recover under 45% compressive strain (true strain), as in the stress–strain curve of the recovery cycle of the ceramic lattice in Figure 2c. During unloading,
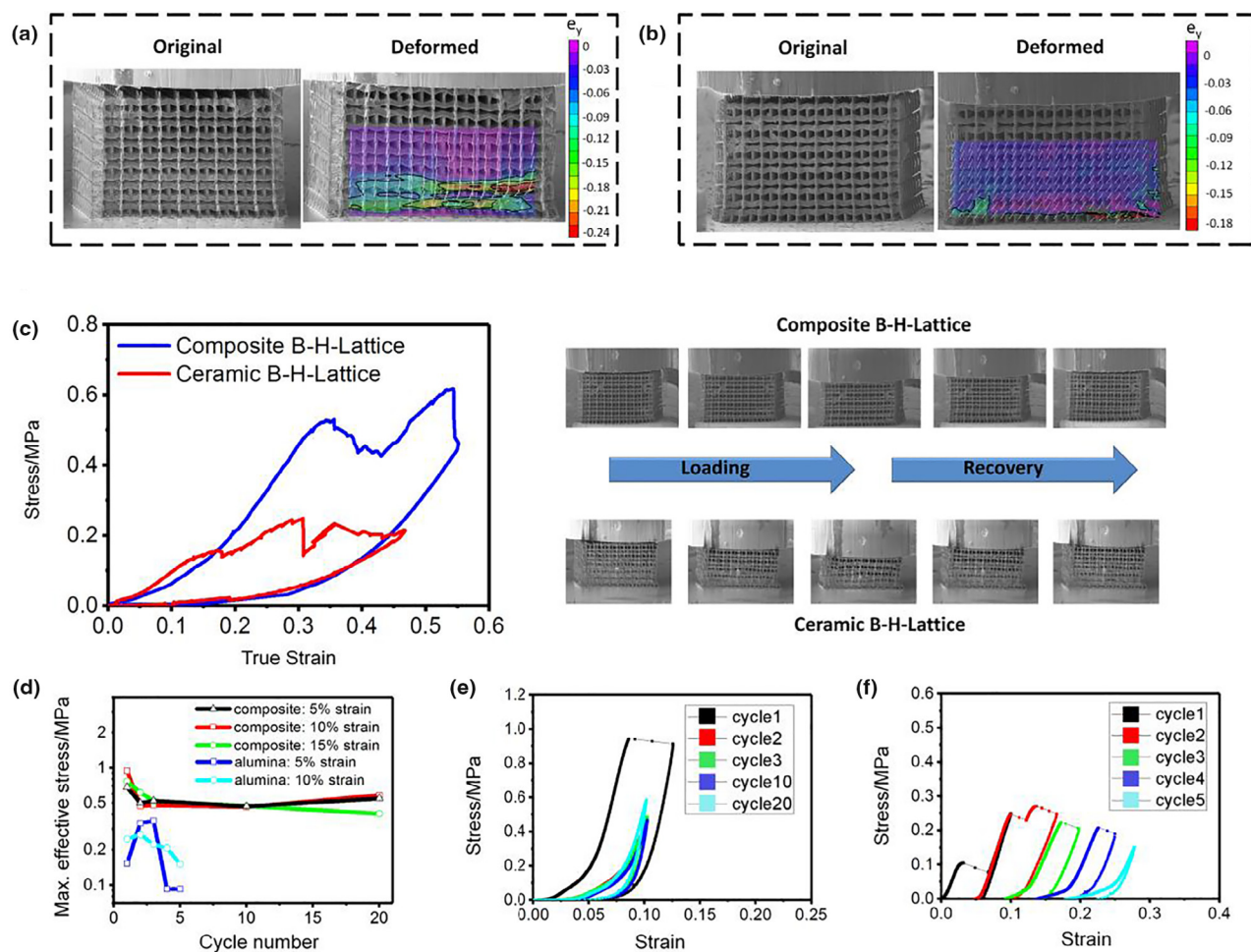
FIGURE 2

Recovery and mechanical cycling performance of the pure ceramic lattice and the composite hollow lattice. (a) Comparison of the side views of a ceramic hollow lattice comprising of a 15-nm alumina nanolayer. The image on the left shows the lattice before compression; the image in the middle shows the lattice during compression. On the right is the accumulated strain map for the compressed lattice, obtained by tracking the pixels from consecutive SEM images. (b) Comparison of the side views of a composite hollow lattice comprising of 15-nm alumina and 8-nm C-PDA nanolayers. The image on the left shows the lattice before compression; the image in the middle shows the lattice during compression. On the right is the accumulated strain map for the compressed lattice. (c) Comparison of the recovery tests of the pure ceramic lattice versus the composite hollow lattice. Prior to the recovery tests, both lattices are pre-indented to remove the free-standing top struts and to activate their recovery mechanisms, i.e., buckling or node deformation. (d) Maximum effective stress of the ceramic and composite lattices during cycling tests. (e) Stress–strain relationship of the composite hollow lattice for 20 cycles at the strain of 10%; (f) stress–strain relationship of ceramic hollow lattice for 5 cycles at the strain of 10%.

the stress/strain curve shows several sharp spikes, indicating structure suffers from mechanical instabilities that could affect the stress response (Supplementary Movie S1). Such mechanical instabilities could be caused by progressive failure, either elastic buckling or cracks, from deformed areas to connected nodes or struts, especially, when the SEM imaging requires stalling of the loading process in an in-situ SEM test.

In contrast, the ceramic/C-PDA B-H-Lattices can recover from a compressive strain of 55%. After unloading, the structure returns to its original position with a smooth stress–strain curve (Figure 2c and Supplementary Movie S2). No necking or buckling is observed, as shown in Figure 2b. As shown in the strain map, strain concentration only occurs between the bottom two stacks of bow-tie units. The effective strain at the bow-tie units is close to 0, while most of the deformation is on the nodes that are mostly hidden in the SEM image. And this is the reason that our digital image correlation software is only able to map the

nodes with high strain concentration partially (bottom right). During compression, adjacent stacks of the unit cells snap to a mismatched position while compressed vertically, as shown by the displacement vectors in the strain map where the upper part of the lattice is moving toward bottom left. The reason for the snap happening is that buckling, as a way of accommodating compressive deformation, is prohibited due to the enhanced buckling strength of the hollow composite struts. The same snapping process occurs between several stacks along the vertical direction, when the lattice is compressed further. Thus, the ceramic/C-PDA nanolayered B-H-Lattice shows zigzag pattern along Z-axis but no distortion in the X-Y dimensions during severe compression (Supplementary Movie S3). Notably, such snapping process is often introducing sharp drops in stress response during in-situ SEM compression (Figure S7a). However, such stress drops would not significantly affect the recoverability. Before collecting the stress–strain curves of the recovery cycles,

lattices have been preloaded for 20% so that the recovery behavior can be best captured.

For the current recoverable microlattices [16,17], which also achieves the recovery from around 50% strains, elastic buckling of the hollow struts is the main mechanism of recovery. Apparently, in the composite B-H lattices presented here, elastic buckling and recovering on hollow struts are no longer the mechanisms for the shape recovery. The elastic deformation mainly resides on the nodes during compression. As the load is released, the lattice will recover with strut rotations. Such deformation mechanism change also affects the stiffness values of the microlattice during loading and unloading. It turns out that the pure ceramic B-H-Lattice has a 'softening' behavior, that after being loaded beyond elastic range, the unloading stiffness of the lattice decreases by 23%, as calculated from the slopes of the stress–strain curves in Figure 2c. The phenomenon of stiffness loss upon the second loading cycle has also been reported in ceramic S-Lattices [16,17], Nickel B-Lattices [19] and tubular carbon foams [39]. The deformation of these cellular structures is all dominated by buckling. On the contrary, in ceramic/C-PDA nanolayered B-H-Lattice, the 'softening' behavior is absent. The stiffness upon unloading even increased 12% compared to loading stiffness, indicating simultaneous elastic and plastic deformations during loading. The loss of stiffness during loading/unloading in pure ceramic B-H-Lattice can be explained by irreversible buckling of the hollow struts. In the ceramic/C-PDA nanolayered B-H-Lattice, because the buckling of the tubular struts is mostly inhibited, the 'softening' effect is thus suppressed.

The cyclability of the ceramic/C-PDA B-H-lattice is compared with that of the pure ceramic B-H-lattice with the same alumina layer thickness, i.e., 15 nm. For the compression of the pure ceramic B-H-lattice, the peak stress drops significantly from 0.35 MPa to 0.09 MPa after 4 cycles at 5% cyclic strain, while at 10 % cyclic strain, the peak stress drops from 0.27 MPa to 0.22 MPa, 0.21 MPa, and 0.15 MPa after 2, 3, and 4 cycles, respectively, as shown in Figure 2d. In addition, the stiffness loss occurs after 3 cycles at the cyclic strain of 5% (Figure S7c) and after 2 cycles at the cyclic strain of 10% (Figure 2f). While several abrupt stress drops occur during the compression, the ceramic lattice fails to recover from each compression cycles and eventually is crushed progressively. At the compression of 15% strain, the ceramic B-H-lattice catastrophically fails at the first cycle. In contrast, the ceramic/C-PDA B-H-lattice shows stable cyclic behavior with significantly higher peak stress level up to 20 cycles of compression at the strain of 5%, 10%, and 15% (Figures 2e, S7d & e). In the meantime, the peak stress from the second compressive cycles at 5% and 10% strains shows no sign of reduction in our experiments. It can be seen that simultaneous elastic and plastic deformations occur in the loading process, which is consistent with our findings in Figure 2c that the stiffness value during unloading would increase compared to that of loading. Under strain of 15%, the stress drops slightly from the second cycle to the 20th cycle, and the lattice shows full recovery and no sign of failure. Typically, the stress–strain curve of the first cycle of the ceramic/C-PDA B-H-Lattice has a plateau after the peak stress is reached. Based on the observation in the in-situ SEM compression test (Supplementary Movies S3 & S5), the plateau corresponds to

the lattice-snapping process triggered by a critical compressive load. It is notable that in the flat punch indentation test, the stress level recorded during the lattice snapping is stable (Figure S7d), while in a SEM compression test, such lattice snapping often is associated with stress drops. The reason is likely to be the different displacement control mechanism in these two tests. For an indenter, the tip transducer displacement is controlled in a load-dependent way, while for a micro-tester compression device inside the SEM, the displacement is controlled by a 3-axis positioning stage as the tip and the load cell is kept static.

Size effect on deformation/failure of B-H-Lattice metamaterials

As shown in the previous section, the ceramic/C-PDA B-H-Lattice has a different deformation mechanism from the pure ceramic B-H-Lattice. The failure of the pure ceramic B-H-lattice is dominated by buckling of the hollow struts. When the buckling occurs, the lattice tends to lose their stiffness quickly resulting in mechanical ruptures. In contrast, struts' buckling is suppressed during compression of ceramic/C-PDA B-H-Lattices, while the deformation is localized at the lattice nodes. In the meantime, the C-PDA nanolayer can stabilize the cracks in the alumina nanolayer during propagation (Figure S5); this will help the hollow nodes withstand large deformation. To better understand the local deformations of the B-H-Lattices and further study the size effect of the ceramic/C-PDA nanolayers, we categorized the deformation within the lattice into 3 types: beam stretching, beam bending, and node bending, as shown in Figure 3a. A similar categorization can be found in the study of general elastic networks [40]. It is often observed in hollow microlattices' compression that the deformation and failure occurs at the nodes of the lattice [16,19]. However, the node-bending mode is often comprised of complex deformation of the shells around the hollow nodes. Therefore, finite element modeling (FEM) is conducted to simulate the deformation of the B-H lattices. FEM results of the elastic deformation of the B-H-Lattice (Figure 3b) suggest that the stress is concentrated at the nodes of the lattice. By tracking the rotational displacement along horizontal struts, we can track the beam-bending and node-bending modes during the lattice compression. Detailed analysis of the bending modes in FEM results can be found in the Figure S9. It is found that when the lattice is comprised of pure ceramic, the node-bending component is absent when the strain is below 1.57%. When the strain exceeds 2.09%, the node-bending component is then increasing rapidly. In contrast, for the composite lattices, both beam bending and node bending are scaling close to linearly with the strain increasing (Table S1).

In Figure 3c, the deformation at lattice nodes of B-H-Lattices with three different material configurations are compared with the FEM results. The node bending causes the nodes to bulge in Y-direction, which is perpendicular to the side wall of the nodes. Moreover, comparing the three material configurations (15 nm Al_2O_3, 15 nm Al_2O_3 + 8 nm C-PDA and 30 nm Al_2O_3 + 8 nm C-PDA), the bulging displacement values and the bulged areas of the ceramic/C-PDA composite nodes are significantly smaller than those of the pure ceramic node. SEM images of the nodes with the three different material configurations are also showing similar morphology, as compared in Figure 3c.
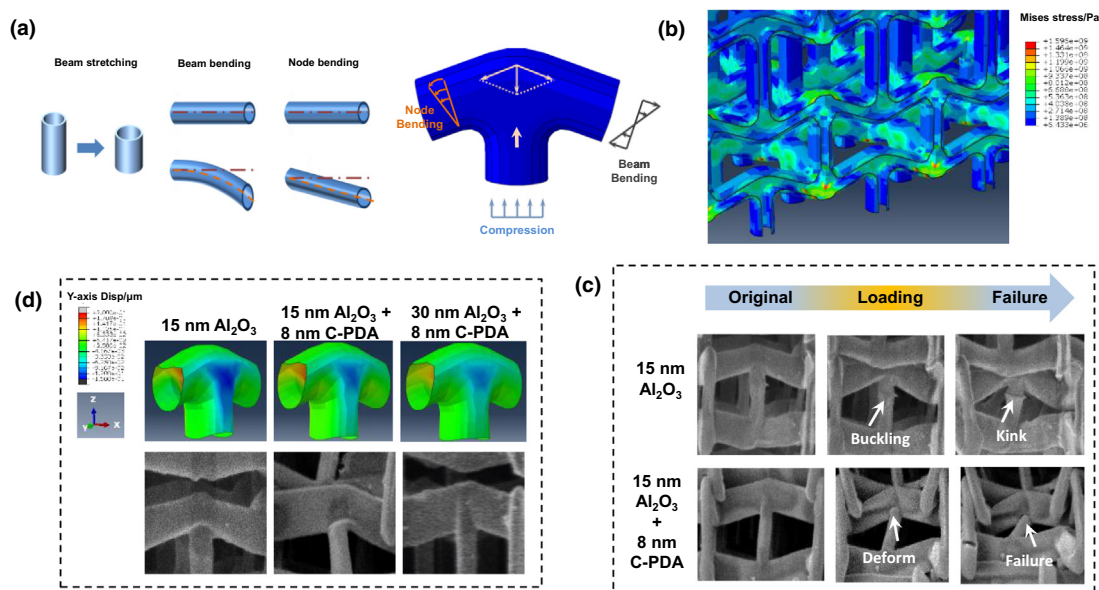
FIGURE 3

Deformation and failure mechanisms of bending-dominated hollow lattices. (a) The deformation induced by uniaxial compression test at the nodes of a lattice can be divided into: beam stretching, beam bending, and node bending. (b) Finite element modeling (FEM) of uniaxial compression of a hollow composite lattice shows that the stress is concentrated at the nodes of the lattice. (c) The bulging hollow nodes from different lattices are shown. The FEM visualizations are taken from a compression at the strain of 2.61%. Below the FEM results are the corresponding experimental observations of the nodes from different lattices. The SEM images are taken at the compressive strain of 33%. (d) Failure at the vertical struts in different lattices is compared. The strut of a ceramic lattice shows bucking and kinking in the middle; while the strut of a composite lattice merely inclines with a crack finally initiated at the spot where the strut is joined with horizontal ones.

For the case of 15 nm Al_2O_3, it can be clearly seen that node bending is causing severe node bulging, whereas, in the case of 15 nm Al_2O_3 + 8 nm C-PDA, the deformation at the lattice node is restricted to the end of the inclined vertical strut. In the case of 30 nm Al_2O_3 + 8 nm C-PDA, no deformation at the lattice node is visible.

The node bending and the bulging at the nodes that caused by it also greatly affects the failure of the lattice. The major failure in ceramic lattices occurs on the vertical hollow struts, which is parallel to the compression direction. As shown in Figure 3d, due to the bulging of the upper node, the compressed hollow strut starts to ovalize in its cross-sectional plane. With further compression, a kink develops in the middle of the strut. Although the ovalization and kinking can also be interpreted as a development of buckling failure, it is worth to note that the geometry imperfection brought by the early deformation of the node accelerates this process. This phenomenon is similar to the previously reported stretching-dominated hollow alumina structures[16]. In contrast, the hollow struts and nodes of the ceramic/C-PDA composite B-H-Lattices do not buckle or bulge till the end of the compression. The large compression along Z-direction is accommodated by inclination of the strut. As a result, the failure spots are localized at the joint where vertical struts are connected to horizontal ones. In many numerical analyses of the hollow microlattice failure, the failure criterion is either that plastic limit is reached or that buckling load is reached for the struts. This method is only suitable when the node is resistant to large deformation. In the case of hollow lattices, especially, when the wall is ultra-thin (a few nanometers), the geometry imperfection brought by node-bending deformation that could

easily lead to early buckling failure should also be considered as a major failure mechanism.

The failure of ceramic/C-PDA B-H-Lattices with thicker (30-nm) ceramic nanolayer is not comparable to the aforementioned two types of lattices. The fracture of such lattices occurs at rather random spots. Cracks initiate without any visible local elastic deformations, indicating a typical brittle failure. A through crack is developed along the direction of 45° from the substrate. The SEM observation of the crack development and stress–strain response are shown in Figure S6. However, at the very early stage of the compression, the lattice can elastically deform by inclination of the vertical struts at the bottom of the lattice (See Supplementary Movie S4). This has never been observed in any ceramic lattices whose hollow struts are made of nanolayers that are thicker than 20 nm. It can be inferred that the C-PDA nanolayer is still playing a role in toughening the 30-nm alumina nanolayer.

Scaling factor in the composite hollow metamaterials
For bending-dominated lattice materials, the modulus is often predicted by the scaling factor of 2:

$$\frac{E}{E_s} \propto \left(\frac{\rho}{\rho_s}\right)^2 \tag{1}$$

Such scaling relationship is relying on several assumptions. Firstly, the constituting struts are solid, rendering the relative density of the lattice dictated by the aspect ratio of the struts. Secondly, ideal bending is the only way of deformation in the bending-dominated lattices. These assumptions are no longer practical in hollow lattices. Therefore, the scaling relationship

should be reconsidered. As calculated in the Supplementary Materials, if we only consider ideal bending in B-H-Lattices with varied wall thicknesses, the effective modulus will follow

$$\frac{E}{E_s} \propto \frac{\rho}{\rho_s} \qquad (2)$$

Similar relationship of strength over density is also derived by Valdevit et al. [41] in their analytical calculation of hollow microlattice yielding. However, in both FEM and experimental approaches, linear scaling in single-order hollow lattices is not achieved [16,19,20,41]. This means that factors such as node bending followed by node deformation are deteriorating the overall scaling factor of the microlattice materials.

In our work, the modulus scaling factor and strength/density ratio of the ceramic/C-PDA B-H-Lattices are delineated from the stress–strain relationship during flat punch indentation (Figure S7d). Based on the measured modulus and strength values of the lattices, the modulus scaling factor is 1.27, the strength scaling factor is 0.97 and the strength/density ratio is 33.6 kPa·kg^{-1}·m^3. Such close-to-ideal scaling factor and high strength/density ratio have only been previously reported in stretching-dominated lattices, but not in any bending-dominated lattices or foams, as in Figure 4a–c. In the meantime, the cyclability of the ceramic/C-PDA B-H-Lattices in this work is the highest among all the current nanolattices (Figure 4d). While most the of the nano-lattices survive for only 1–6 cycles,
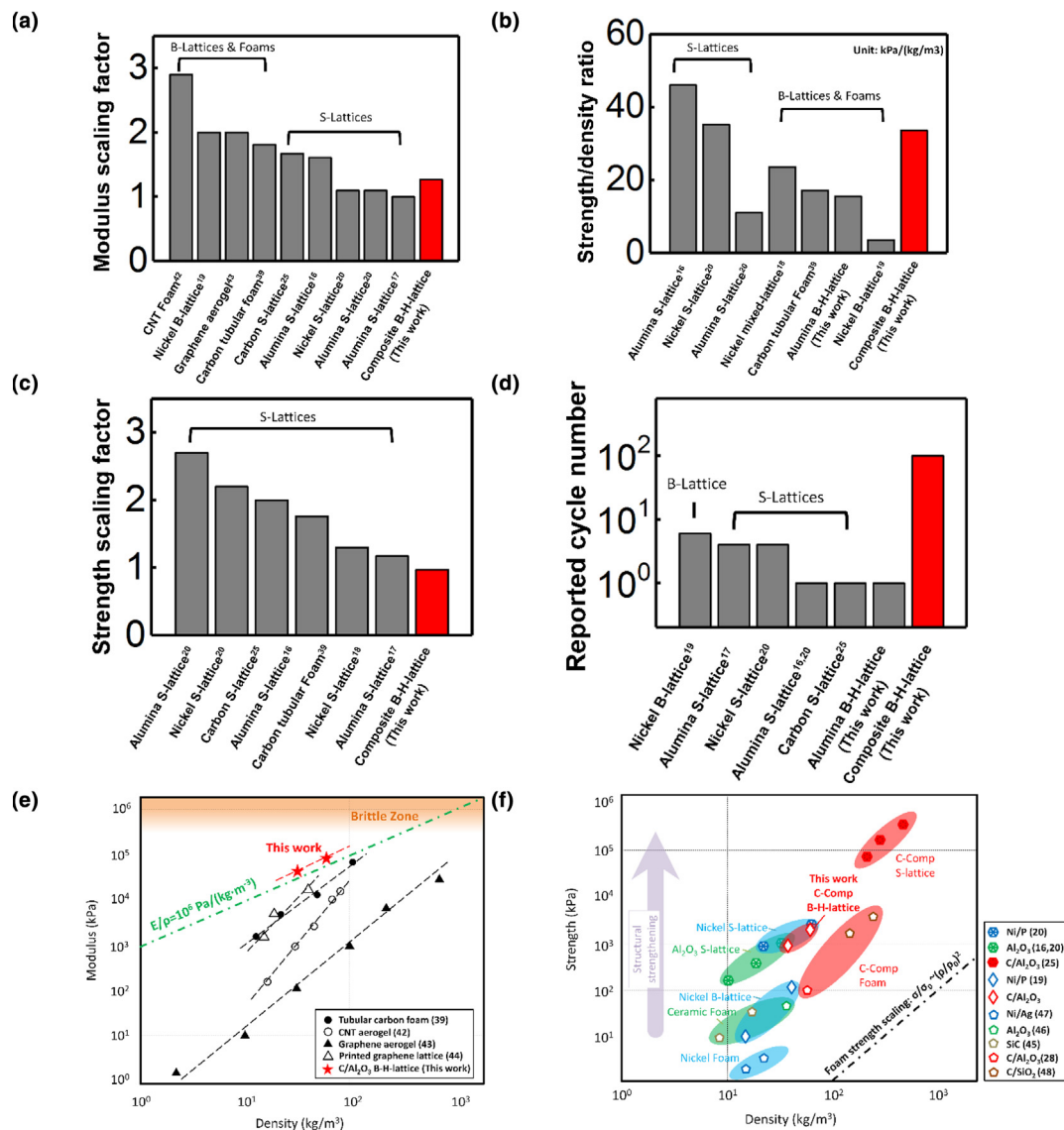
FIGURE 4

Comparison of mechanical properties of the composite lattice versus the other cellular materials. (a) The histogram is showing the modulus scaling factors of different cellular materials. (b) The histogram is showing the strength scaling factors of different cellular materials. (c) The histogram is showing the strength over mass density ratio of different cellular materials. (d) The histogram is showing the reported cyclic ability of different cellular materials. The density range is chosen as 10–100 kg/m^3. (e) Compared to other carbon-based cellular foams, the composite hollow lattices in this work have a modulus to density ratio over 10^6 Pa/(kg·m^{-3}); (f) If all ceramic, metal, and carbon composite cellular materials are categorized into three: (i) foams; (ii) bending-dominated lattices (B-lattices); (iii) stretching-dominated lattices (S-lattices). Generally, the strength sequence is 'Foam < B-lattices < S-lattices'. Our composite B-lattices are nearly matching metal or ceramic S-lattices in strength at similar mass densities.

RESEARCH: Short Communication

including S-Lattices (alumina [16,17,20], nickel [20], carbon [25]) and B-Lattices (nickel [19] and alumina-B-H-Lattice in this study), the ceramic/C-PDA B-H-Lattices show much superior recoverability after 100 of cycles under 5–15% strains. In Figure 4d, the effective modulus of the composite B-H-Lattices is compared to the existing highly recoverable carbon-based foams [39,42–44]. The modulus/mass efficiency is elevated above 10^6 Pa/(kg·m^{-3}), which is much superior to the pure carbon-based foams. It is worth noting that the deformations of nearly all carbon foams rely on planar or shell buckling, the deformation of composite B-H-Lattices resides on the deformation of the hollow lattice nodes. Such difference results in lower scaling factors for the composite B-H-Lattice. In Figure 4e, the most typical cellular structures made of ceramic, metal, and carbon composite reported so far are compared regarding their strength. The trend of structural strengthening effect can be clearly seen for metal, ceramic, and carbon composite cellular materials. Three main types of cellular structure are included in this Ashby plot: foams, B-lattices, and S-lattices. Generally, at a certain mass density (e.g., 10–100 kg/m^3 in this paper), strengths of ceramic and metal cellular materials follow: Foam [45–47] < B-Lattice[19] < S-Lattice [16,20]. It can be seen from the plot that the composite B-H-Lattice in this work nearly matches the strength of S-Lattice of metal and ceramic in the density range of 10–100 kg/m^3. On the other hand, carbon composite cellular structures in such light-weight regime are never reported with a superior strength. Although existing carbon composite foams [28,48] and solid lattices [25] already exhibit outstanding mechanical strength, their mass density is approximately an order higher, and they are faced with brittle failure. The superior property in the B-H-Lattices is mainly due to and coupling of ceramic and C-PDA nanolayers, which suppress the node bending and strut buckling during large compressive deformation. In a broader view, the composite bending hollow nanolattice provides a path-finding concept to take advantage of the high stiffness/strength from the ceramic, while its brittle nature is suppressed by the carbonized polymer.

Conclusion

A unique ceramic/C-PDA nanolayered composite bending-dominated hollow lattice (B-H-lattice) is developed for the first time, with recoverability, high strength/weight ratio, optimal scaling factor, and good cyclic performance. The deformation behavior of the ceramic hollow lattices is changed significantly by coherently depositing a few nanometers of carbonized mussel-inspired bio-polymer (C-PDA). While the deformation of the pure ceramic lattice is dominated by buckling, such failure mechanism is significantly suppressed in the composite B-H-lattice. In the meantime, despite the buckling-recovery behavior of the pure ceramic lattices, the composite B-H-lattices have a new recovery mechanism of elastic node bending. The recoverable strain reaches 55%. Furthermore, the composite B-H-lattice shows stable cyclic-loading behavior under up to 15% compressive strain. In terms of scaling factors and strength/density ratio, the ceramic/C-PDA B-H-Lattice outperforms most of the nano-carbon-based cellulose structures and B-Lattice metamaterials and is comparable to those of the S-Lattice metamaterials. Such

combined properties of stiffness/strength/recovery/cyclability within node-bending lattices have not been observed before in any B-Lattice or S-Lattice metamaterials. This study illustrates that stable node bending and suppressed strut buckling are the key factors to improve the mechanical performances of bending-dominated nanolattice metamaterials. The fabrication of such multi-material lattices can potentially be scaled up once convenient deposition method like solution-based PDA coating used in this work can extend to ceramics. The unique B-H-Lattice design can be quickly applied to many mechanical applications, such as energy dissipation, damping, etc., with reliable and robust performances.

Appendix A. Supplementary data

Supplementary data associated with this article can be found, in the online version, at https://doi.org/10.1016/j.mattod.2018.03.027.

References

[1] V.P. Veedu et al., Nat. Mater. 5 (6) (2006) 457.
[2] A. Yu et al., J. Phys. Chem. C 111 (21) (2007) 7565.
[3] F.T. Moutos et al., Nat. Mater. 6 (2) (2007) 162.
[4] B. Jin et al., Electrochem. Commun. 10 (10) (2008) 1537.
[5] P.C. Ramamurthy et al., Solid-State Electron. 48 (10–11) (2004) 2019.
[6] K. Byungkyu et al., Smart Mater. Struct. 14 (6) (2005) 1579.
[7] E. Munch et al., Science 322 (5907) (2008) 1516.
[8] L.S. Dimas, M.J. Buehler, J. Mater. Res. 28 (10) (2013) 1295.
[9] F. Bouville et al., Nat. Mater. 13 (5) (2014) 508.
[10] U.G. Wegst et al., Nat. Mater. 14 (1) (2015) 23.
[11] L.J. Gibson, J. Biomech. 38 (3) (2005) 377.
[12] N.A. Fleck et al., Phys. Eng. Sci. 466 (2121) (2010) 2495.
[13] D. Lin et al., ACS Nano 8 (10) (2014) 9710.
[14] R.L. Truby, J.A. Lewis, Nature 540 (7633) (2016) 371.
[15] T.A. Schaedler, W.B. Carter, Annu. Rev. Mater. Res. 46 (1) (2016) 187.
[16] L.R. Meza et al., Science 345 (6202) (2014) 1322.
[17] L.R. Meza et al., Proc. Natl. Acad. Sci. 112 (37) (2015) 11502.
[18] X. Zheng et al., Nat. Mater. (2016). advance online publication.
[19] T.A. Schaedler et al., Science 334 (6058) (2011) 962.
[20] X. Zheng et al., Science 344 (6190) (2014) 1373.
[21] L.R. Meza, J.R. Greer, J. Mater. Sci. 49 (6) (2014) 2496.
[22] J.-H. Lee et al., Adv. Mater. 24 (36) (2012) 4782.
[23] K. Davami et al., Nat. Commun. (2015) 6.
[24] M.F. Ashby, Series A, Math., Phys., Eng. Sci. 364 (1838) (2006) 15.
[25] J. Bauer et al., Nat. Mater. 15 (4) (2016) 438.
[26] Y. Jiang, Q. Wang, Sci. Rep. 6 (2016) 34147.
[27] A.G. Evans et al., Int. J. Impact Eng. 37 (9) (2010) 947.
[28] Zhang, Q., et al., Adv. Mater., n/a. .
[29] J. Bauer et al., Proc. Natl. Acad. Sci. 111 (7) (2014) 2453.
[30] M. Mieszala et al., Small (2016).
[31] H. Lee et al., Science 318 (5849) (2007) 426.
[32] V. Ball et al., J. Colloid Interface Sci. 386 (1) (2012) 366.
[33] B.P. Lee et al., Annu. Rev. Mater. Res. 41 (1) (2011) 99.
[34] B. Li et al., Langmuir 25 (13) (2009) 7368.
[35] J. Ou et al., Surf. Interface Anal. 43 (4) (2011) 803.
[36] Y.S. Lee et al., Sci. Rep. 6 (2016) 22650.
[37] C.M. Parnell et al., Sci. Rep. 6 (2016) 31415.
[38] S. Li et al., Nature 539 (7630) (2016) 541.
[39] H. Bi et al., Adv. Mater. 27 (39) (2015) 5943.
[40] G. Gurtner, M. Durand, Procd. Royal Soc. A: Math., Phys. Eng. Sci. 470 (2014) 2164.
[41] L. Valdevit et al., J. Mater. Res. 28 (17) (2013) 2461.
[42] M.A. Worsley et al., Appl. Phys. Lett. 94 (7) (2009) 073115.
[43] Q. Zhang et al., Adv. Mater. 28 (11) (2016) 2229.
[44] C. Zhu et al., Nat. Commun. 6 (2015) 6962.
[45] S. Chabi et al., ACS Nano 10 (2) (2016) 1871.
[46] J.F. Poco et al., J. Non-Cryst. Solids 285 (1–3) (2001) 57.
[47] B. Jiang et al., Sci. Rep. 5 (2015) 13825.
[48] M. Moner-Girona et al., Appl. Phys. A 74 (1) (2002) 119.